Ferrocene-conjugated Copper(II) Complexes of L-Methionine and Phenanthroline Bases: Synthesis, Structure and Photocytotoxic Activity

Tridib K. Goswami,[†] Sudarshan Gadadhar,[‡] Mithun Roy,[†] Munirathinam Nethaji,[†] Anjali A. Karande,*[,‡] and Akhil R. Chakravarty*[,†]

[†]*Department of Inorganic and Physical Chemistry, Indian Institute of Science, Bangalore 560012, India*

[‡]*Department of Biochemistry, Indian Institute of Science, Bangalore 560012, India*

Supplementary Data

Corresponding authors. E-mail: anjali@biochem.iisc.ernet.in, Fax: 91-80-23600814 (AAK) and E-mail: arc@ipc.iisc.ernet.in, Fax: 91-80-23600683 (ARC)

Table S1. Selected bond distances (Å) and bond angles (º) of [Cu(Ph-met)(phen)](ClO_4) (**5a**)

Cu(1)–O(1)	1.934(3)	O(1)–Cu(1)–N(3)	82.15(16)
Cu(1)–O(2′)	2.220(4)	O(1)–Cu(1)–O(2′)	91.25(15)
Cu(1)–N(1)	2.019(5)	N(1)–Cu(1)–N(3)	152.76(18)
Cu(1)–N(2)	1.994(5)	N(1)–Cu(1)–O(2′)	99.70(16)
Cu(1)–N(3)	2.039(4)	N(2)–Cu(1)–N(1)	82.54(18)
O(1)–Cu(1)–N(1)	94.78(16)	N(2)–Cu(1)–O(2′)	89.51(16)
O(1)–Cu(1)–N(2)	177.30(18)	N(2)–Cu(1)–N(3)	100.10(18)
		N(3)–Cu(1)–O(2′)	107.40(16)

Symmetry transformation for O(2′): x-1/2, -y+3/2, -z+2.

Table S2. IC_{50} values of the ligands in HeLa and MCF-7 Cells

Compound	HeLa		MCF-7	
	IC_{50} (μM) dark[a]	IC_{50} (μM) visible light[b]	IC_{50} (μM) dark[a]	IC_{50} (μM) visible light[b]
Fc-metH	>200	>200	>200	>200
Ph-metH	>200	>200	>200	>200
phen	>200	186.7 ± 4.0	131.8 ± 2.0	115.2 ± 2.0
dpq	>200	>200	108.8 ± 2.0	93.5 ± 3.0
dppz	>200	52.3 ± 0.8	96.6 ± 1.0	77.8 ± 2.0
nip	76.86 ± 1.20	47.88 ± 1.04	62.38 ± 1.18	35.6 ± 0.9
$Cu(NO_3)_2{\cdot}3H_2O$	>200	169.0 ± 4.0	-	-

[a] The IC_{50} values correspond to 24 h incubation in dark. [b] The IC_{50} values correspond to 4 h incubation in dark followed by photo-exposure to visible light (400-700 nm, 10 *J* cm^{-2}).

Table S3. Selected Crystallographic Data for the complex [Cu(Ph-met)(phen)](ClO_4) (**5a**)

	[Cu(Ph-met)(phen)](ClO_4) (**5a**)
Empirical formula	$C_{24}H_{24}ClCuN_3O_6S$
Fw, g M^{-1}	581.51
Crystal system	Orthorhombic
Space group	$P2_12_12_1$
a, Å	7.4256(7)
b, Å	11.2727(10)
c, Å	29.133(3)
α, °	90
β, °	90
γ, °	90
V, $Å^3$	2438.6(4)
Z	4
T, K	293(2)
ρ_{calcd}, g cm^{-3}	1.584
λ, Å (Mo-K_α)	0.71073
μ, cm^{-1}	1.137
Data / restraints / parameters	7357 / 0 / 325
F(000)	1196
Goodness-of-fit	0.861
R (F_o)[a], I>2σ(I) [wR (F_o)[b]]	0.0613 [0.1449]
R (all data) [wR (all data)]	0.1552 [0.1905]
Largest diff. peak and hole (e $Å^{-3}$)	0.705, -0.421

[a]$R = \Sigma||F_o|-|F_c||/\Sigma|F_o|$, [b]$wR = \{\Sigma[w(F_o^2-F_c^2)^2]/\Sigma[w(F_o)^2]\}^{½}$; $w = [\sigma^2(F_o)^2 + (AP)^2 + BP]^{-1}$, where $P = (F_o^2 + 2F_c^2)/3$, A = 0.1095; B = 0.

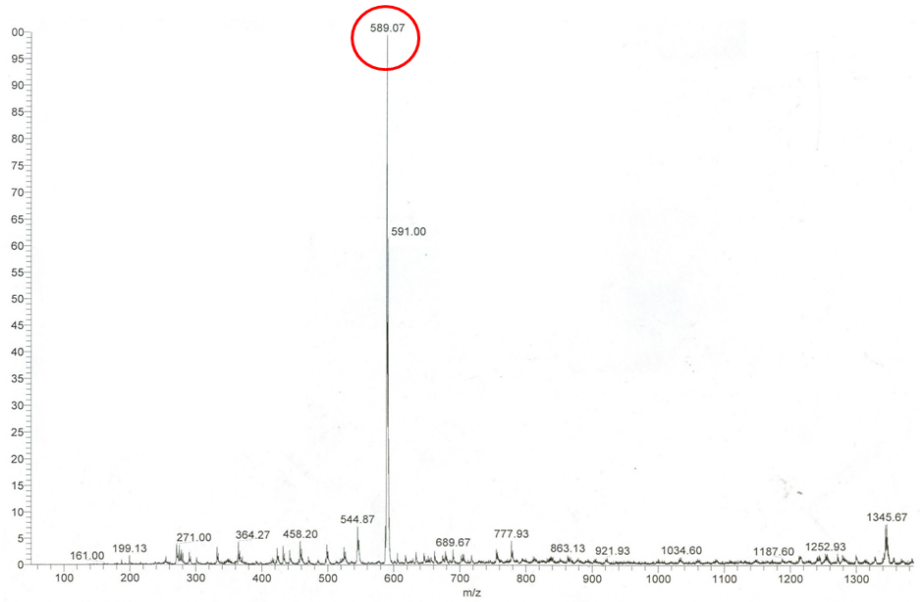

Figure S1. The ESI-MS spectrum of [Cu(Fc-met)(phen)](NO_3) (**1**) in aqueous MeOH showing prominent parent ion peak at 589.07 (m/z) which corresponds to $[M-(NO_3^-)]^+$. The peak at 591 m/z unit is due to the isotopic abundance of ^{65}Cu.

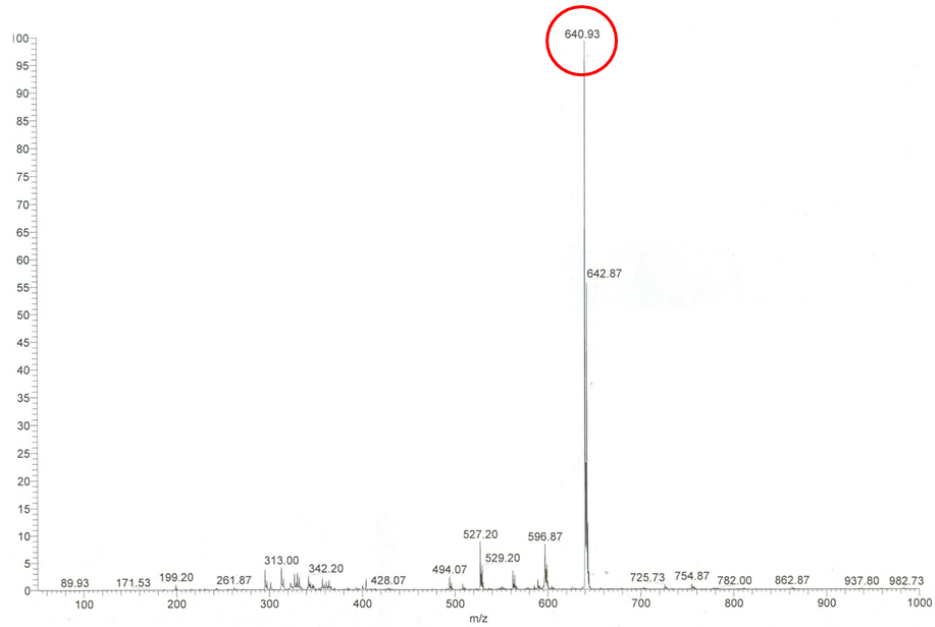

Figure S2. The ESI-MS spectrum of [Cu(Fc-met)(dpq)](NO_3) (**2**) in aqueous MeOH showing prominent parent ion peakat 640.93 (m/z) which corresponds to $[M-(NO_3^-)]^+$. The peak at ~2 m/z unit higher at 642.87 is due to the isotopic abundance of ^{65}Cu.

Figure S3. The ESI-MS spectrum of [Cu(Fc-met)(dppz)](NO_3) (**3**) in aqueous MeOH showing prominent parent ion peakat 691 (m/z) which corresponds to $[M-(NO_3^-)]^+$. The peak at 693 m/z is due to the isotopic abundance of ^{65}Cu.

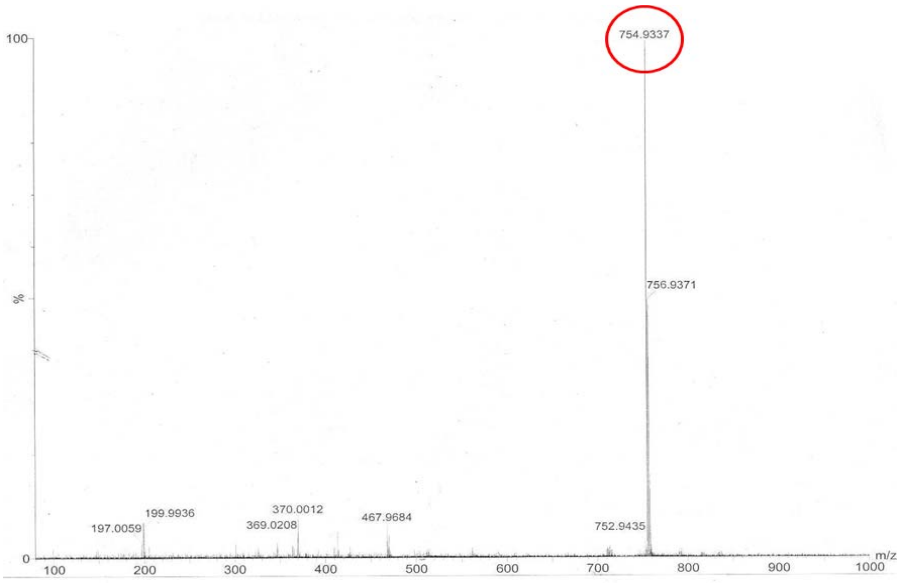

Figure S4. The ESI-MS spectrum of [Cu(Fc-met)(nip)](NO_3) (**4**) in aqueous MeOH showing prominent parent ion peak(m/z) at 754.93 which corresponds to $[M-(NO_3^-)]^+$. The peak at 756.94 m/z unit is due to the isotopic abundance of ^{65}Cu.

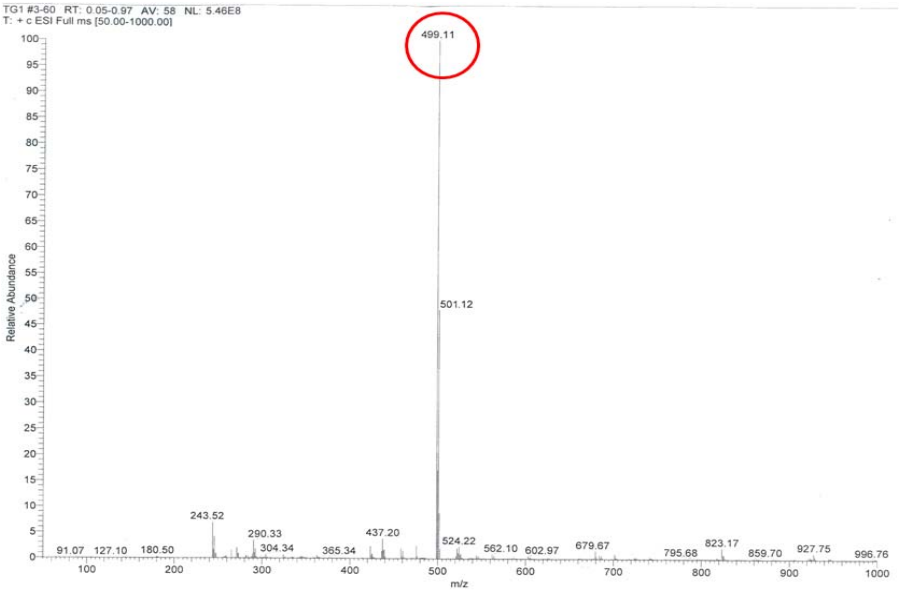

Figure S5. The ESI-MS spectrum of [Cu(ph-met)(phen)](NO_3) (**5**) in aqueous MeOH showing prominent parent ion peak(m/z) at 499.11 which corresponds to $[[(M+H_2O)-(NO_3^-)]^+$.

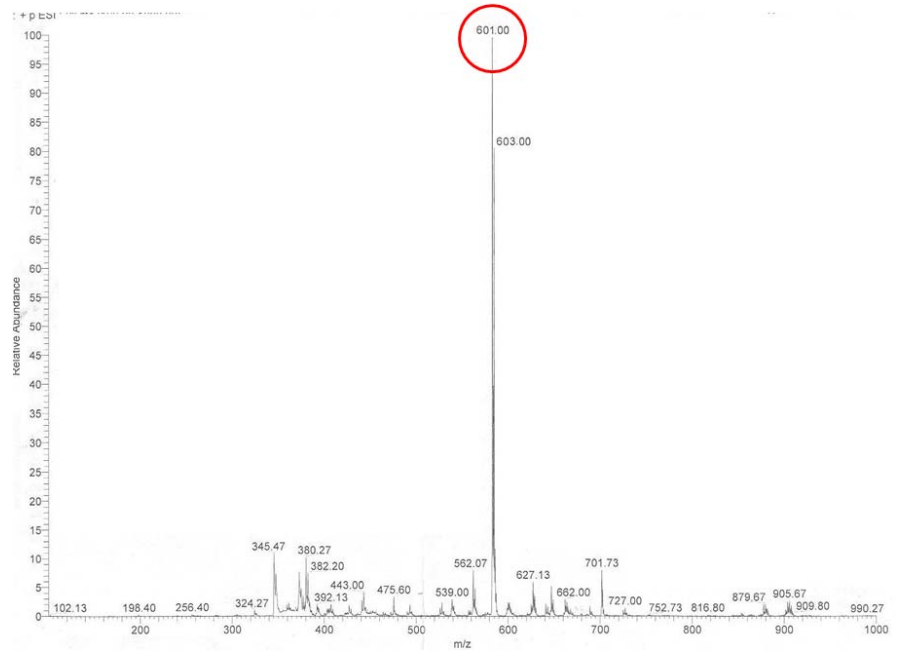

Figure S6. The ESI-MS spectrum of [Cu(Ph-met)(dppz)](NO_3) (**6**) in aqueous MeOH showing prominent parent ion peak(m/z) at 601 which corresponds to $[(M+H_2O)-(NO_3^-)]^+$. The peak at 603 m/z is due to the isotopic abundance of ^{65}Cu.

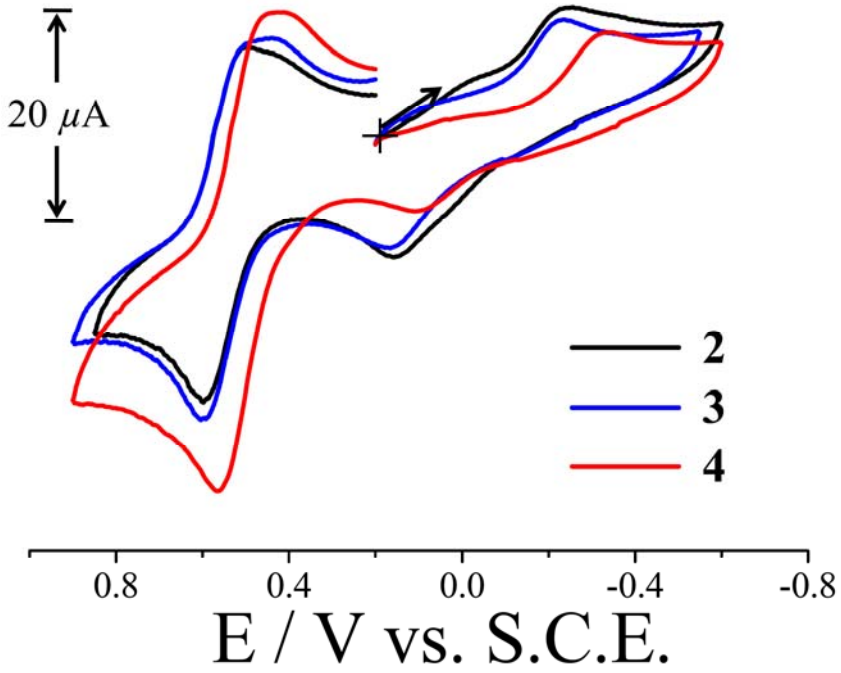

Figure S7. Cyclic voltammograms of the complexes **2-4** in DMF-0.1 M TBAP at a scan rate of 50 mV s^{-1}.

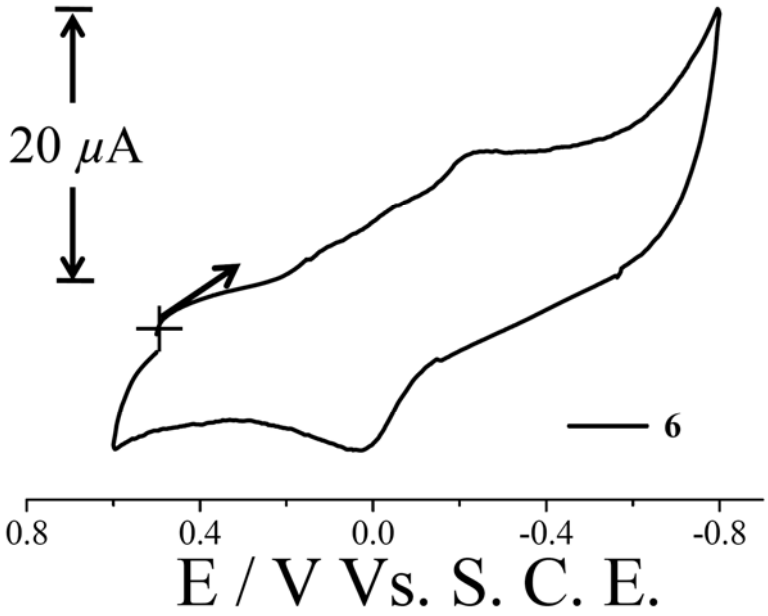

Figure S8. Cyclic voltammogram of complex **6** showing the Cu(II)-Cu(I) redox couple in DMF-0.1 M TBAP at a scan rate of 50 mV s^{-1}.

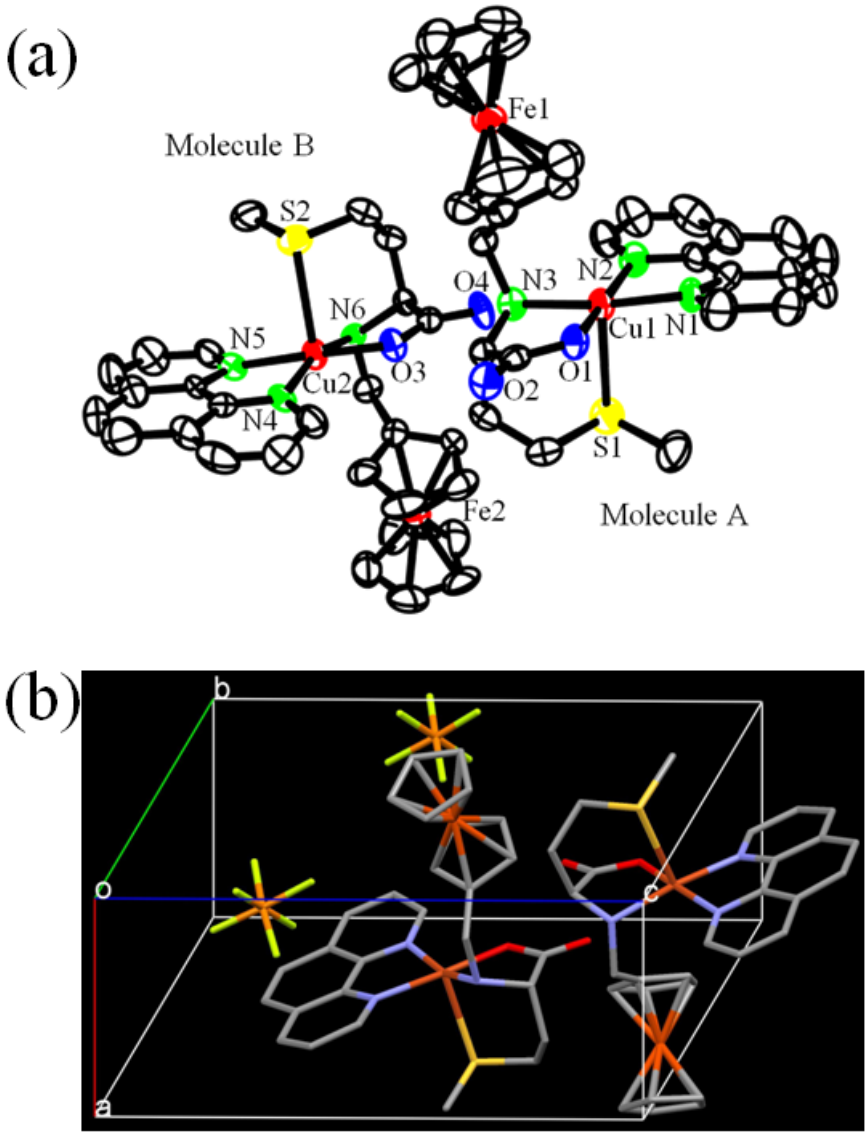

Figure S9. (a) An ORTEP view of the cationic complex in [Cu(Fc-Met)(phen)](PF_6) (**1a**) showing 50% probability thermal ellipsoids and the atom numbering scheme for the metal and hetero atoms. The hydrogen atoms are omitted for clarity. Atoms color code: Fe and Cu, red; O, blue; N, green; C, black. (b) Unit cell packing diagram for the complex [Cu(Fc-met)(phen)](PF_6) (**1a**). The hydrogen atoms are not shown for clarity.

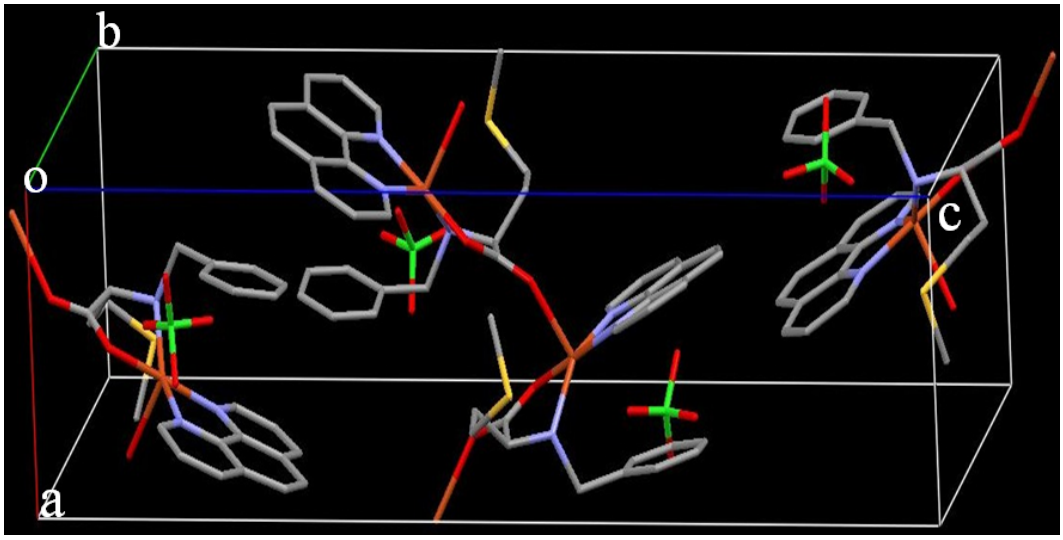

Figure S10. Unit cell packing diagram of the complex [Cu(Ph-met)(phen)](ClO_4) (**5a**). The hydrogen atoms are not shown for clarity.

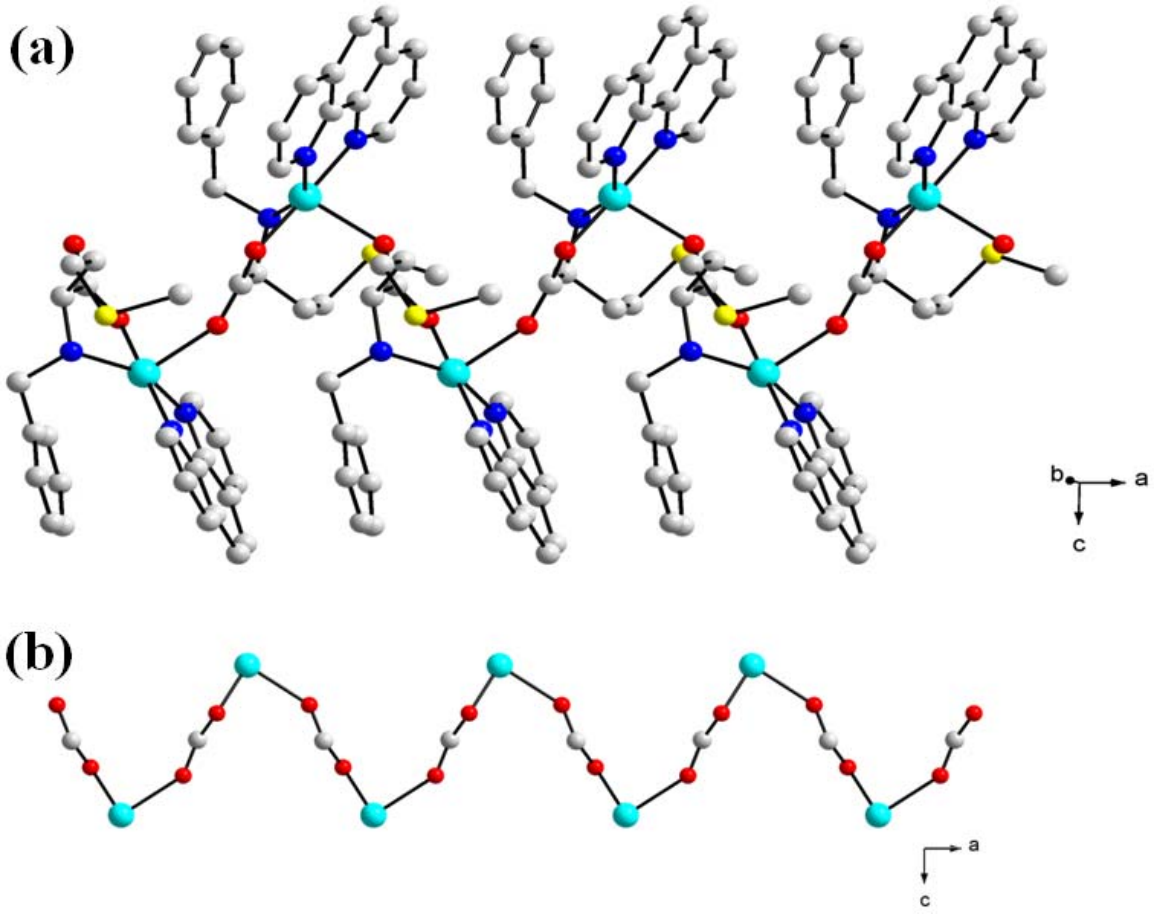

Figure S11. Crystal packing pattern of the complex [Cu(Ph-met)(phen)](ClO_4) (**5a**): (a) 1-D chain showing the stacking of the phenyl ring in between the phenanthroline bases; (b) simplified 1-D pattern of the chain structure showing only the metal and the bridging carboxylate moiety. The hydrogen atoms are not shown for clarity.

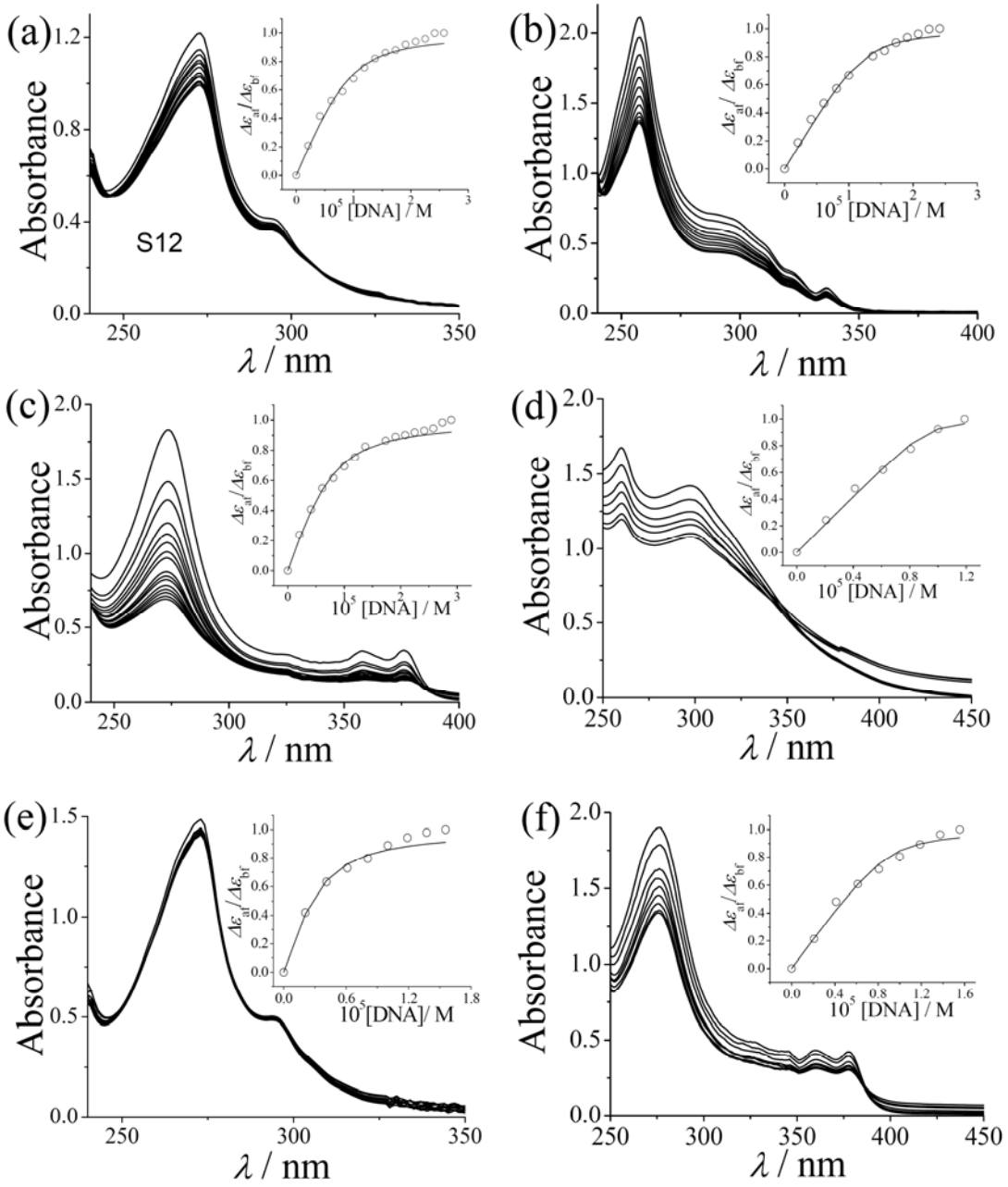

Figure S12. Absorption spectral traces of the complexes **1** (a), **2** (b), **3** (c), **4** (d), **5** (e) and **6** (f) in 5 mM Tris-HCl buffer (pH 7.2) on increasing the quantity of calf thymus DNA. The inset shows the least-squares fits of $\Delta\varepsilon_{af}/\Delta\varepsilon_{bf}$ vs. [DNA] for the complexes using McGhee-von Hippel (MvH) method using the expression of Bard and co-workers (vide text for details).

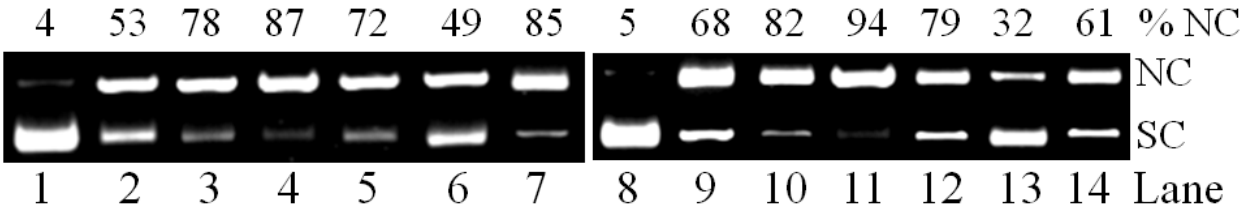

Figure S13. Gel electrophoresis diagram showing the chemical nuclease activity of the complexes **1-6** (10 μM) using SC pUC19 DNA (0.2 μg, 30 μM b.p.) in the presence of 1 mM Glutathione (GSH) as a reducing and 200 μM H_2O_2 as oxidizing agent: lane-1, DNA control; lane-2, DNA + **1** + GSH; lane-3, DNA + **2** + GSH; lane-4, DNA + **3** + GSH; lane-5, DNA + **4** + GSH; lane-6, DNA + **5** + GSH; lane-7, DNA + **6** + GSH; lane-8, DNA control; lane-9, DNA + **1** + H_2O_2; lane-10, DNA + **2** + H_2O_2; lane-11, DNA + **3** + H_2O_2; lane-12, DNA + **4** + H_2O_2; lane-13, DNA + **5** + H_2O_2; lane-14, DNA + **6** + H_2O_2.

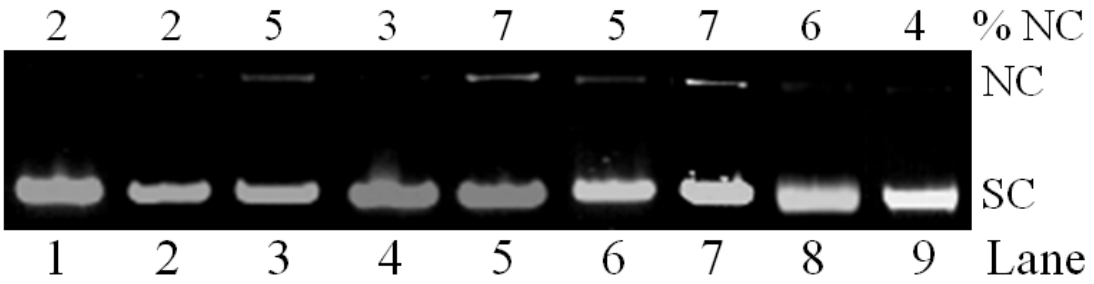

Figure S14. Gel electrophoresis diagram showing the chemical nuclease activity of the Ph-metH, Fc-metH (10 μM) and Cu^{2+} (10 μM) salt using SC pUC19 DNA (0.2 μg, 30 μM b.p.) in the presence of 1.0 mM glutathione (GSH) as a reducing agent and 200 μM H_2O_2 as an oxidizing agent. Details are given in a tabular form.

Lane No.	Reaction Conditions	Incubation Time in dark (t/h)	% NC
1	DNA control	2	2
2	DNA + GSH	2	2
3	DNA + H_2O_2	2	5
4	DNA + Ph-metH + GSH	2	3
5	DNA + Fc-metH + GSH	2	7
6	DNA + Ph-metH + H_2O_2	2	5
7	DNA + Fc-metH + H_2O_2	2	7
8	DNA + $Cu(NO_3)_2 \cdot 3H_2O$ + GSH	2	6
9	DNA + $Cu(NO_3)_2 \cdot 3H_2O$ + H_2O_2	2	4

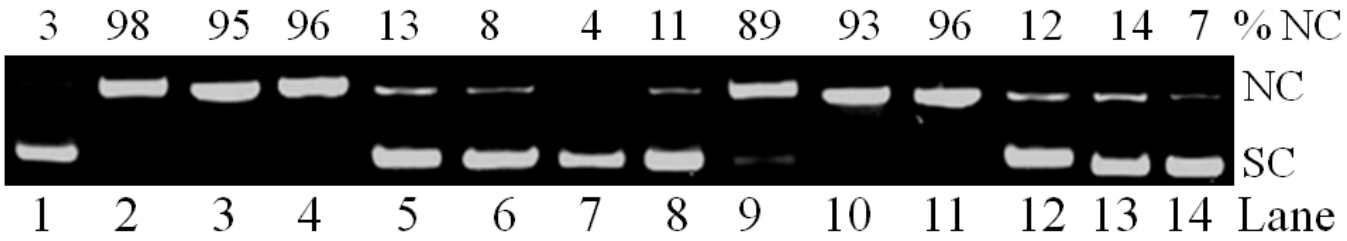

Figure S15. Gel diagram showing the mechanistic aspects of chemical nuclease activity of [Cu(Fc-met)(dppz)](NO_3) (**3**) in the presence of various singlet oxygen quenchers and hydroxyl radical scavengers using GSH and H_2O_2 as the external reducing and oxidizing agents.

Lane No.	Reaction conditions	Incubation time in dalk (t/h)	% NC
1	DNA control	2	3
2	DNA + **3** + GSH	2	98
3	DNA + **3** + NaN_3 + GSH	2	95
4	DNA + **3** + TEMP + GSH	2	96
5	DNA + **3** + DMSO + GSH	2	13
6	DNA + **3** + KI + GSH	2	8
7	DNA + **3** + Catalase + GSH	2	4
8	DNA + **3** + Argon + GSH	2	11
9	DNA + **3** + H_2O_2	2	89
10	DNA + **3** + NaN_3 + H_2O_2	2	93
11	DNA + **3** + TEMP + H_2O_2	2	95
12	DNA + **3** + DMSO + H_2O_2	2	12
13	DNA + **3** + KI + H_2O_2	2	14
14	DNA + **3** + Argon + H_2O_2	2	7

Figure S16. Gel electrophoresis diagram showing the chemical nuclease activity of the complexes **1-3** (10 μM) using SC pUC19 DNA (0.2 μg, 30 μM b.p.) in the presence of 1.0 mM glutathione (GSH) as a reducing agent and distamycin as minor groove and methyl green as major groove binder. Details are given in a tabular form.

Lane No.	Reaction conditions	Incubation time in dalk (t/h)	% NC
1	DNA control	2	3
2	DNA + **1** + GSH	2	55
3	DNA + **2** + GSH	2	78
4	DNA + **3** + GSH	2	89
5	DNA + distamycin + **1** + GSH	2	12
6	DNA + distamycin + **2** + GSH	2	13
7	DNA + distamycin + **3** + GSH	2	87
8	DNA + methyl green + **1** + GSH	2	53
9	DNA + methyl green + **2** + GSH	2	76
10	DNA + methyl green + **3** + GSH	2	14
11	DNA + distamycin	2	5
12	DNA + methyl green	2	8

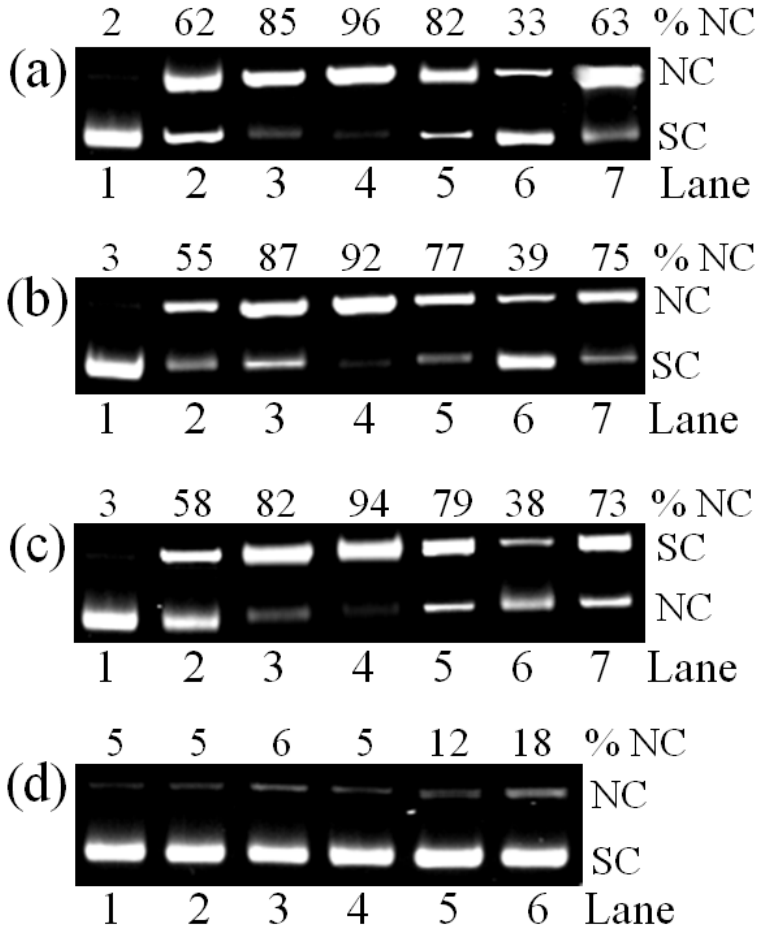

Figure S17. Gel electrophoresis diagram showing the photo-induced DNA cleavage activity of the complexes **1**-**6** (20 μM for 454 nm and 25 μM for other wavelengths) using SC pUC19 DNA (0.2 μg, 30 μM b.p.) on exposure to monochromatic laser radiations for 2 h. (a) 454 nm: lane-1, DNA control; lane-2, DNA + **1**; lane-3, DNA + **2**; lane-4, DNA + **3**; lane-5, DNA + **4**; lane-6, DNA + **5**; lane-7, DNA + **6**. (b) 568 nm: lane-1, DNA control; lane-2, DNA + **1**; lane-3, DNA + **2**; lane-4, DNA + **3**; lane-5, DNA + **4**; lane-6, DNA + **5**; lane-7, DNA + **6**. (c) 647 nm: lane-1, DNA control; lane-2, DNA + **1**; lane-3, DNA + **2**; lane-4, DNA + **3**; lane-5, DNA + **4**; lane-6, DNA + **5**; lane-7, DNA + **6**. (d) Dark: lane-1, DNA + **1**; lane-2, DNA + **2**; lane-3, DNA + **3**; lane-4, DNA + **4**; lane-5, DNA + **5**; lane-6, DNA + **6**.

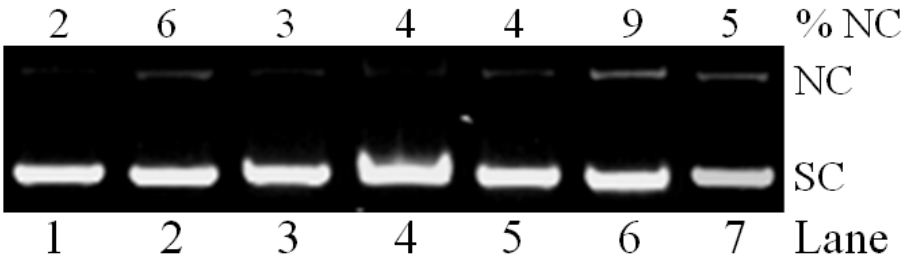

Figure S18. Gel electrophoresis diagram showing the photocleavage of SC pUC19 DNA (0.2 μg, 30 μM bp) by the ligands on irradiation with 647 nm laser radiation (50 mW). Exposure time (t) = 2h. Details are given below in a tabular form.

Lane No.	Reaction Conditions	[Ligand] / μM	λ / nm	% NC
1	DNA control	25	647	2
2	DNA + Ph-trpH	25	647	6
3	DNA + Fc-trpH	25	647	3
4	DNA + phen	25	647	4
5	DNA + dpq	25	647	4
6	DNA + dppz	25	647	9
7	DNA + nip	25	647	5

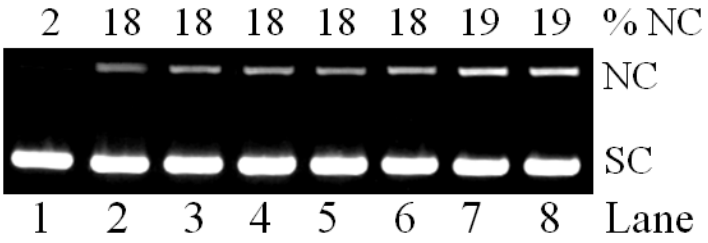

Figure S19. Gel diagram showing the nuclease activity of [Cu(Ph-met)(dppz)](NO_3) (**6**) in dark for 2 h in the presence of various singlet oxygen quenchers and hydroxyl radical scavengers using GSH and H_2O_2 as the external reducing and oxidizing agents: lane-1, DNA control; lane-2, DNA + **6**; lane-3, DNA + **6** + NaN_3; lane-4, DNA + **6** + TEMP; lane-5, DNA + **6** + L-His; lane-6, DNA + **6** + DMSO; lane-7, DNA + **6** + KI; lane-8, DNA + **6** + Catalase.

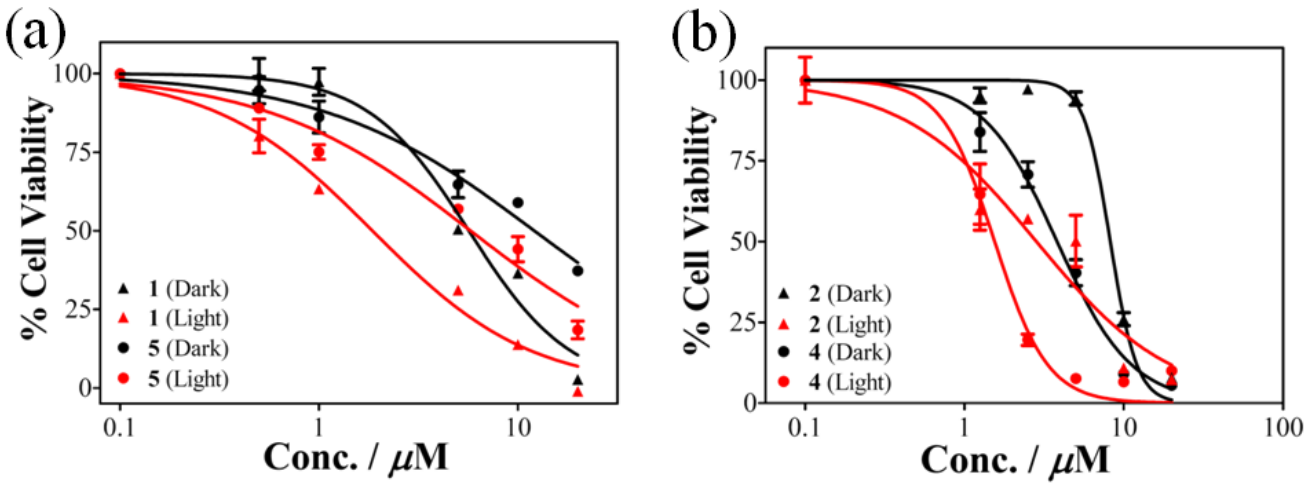

Figure S20. Cell viability plots showing cytotoxic effect of (a) complexes **1** and **5** and (b) complexes **2** and **4** in HeLa cells in dark (black symbols) and in the presence of visible light (red symbols, 400-700 nm, 10 J cm^{-2}).

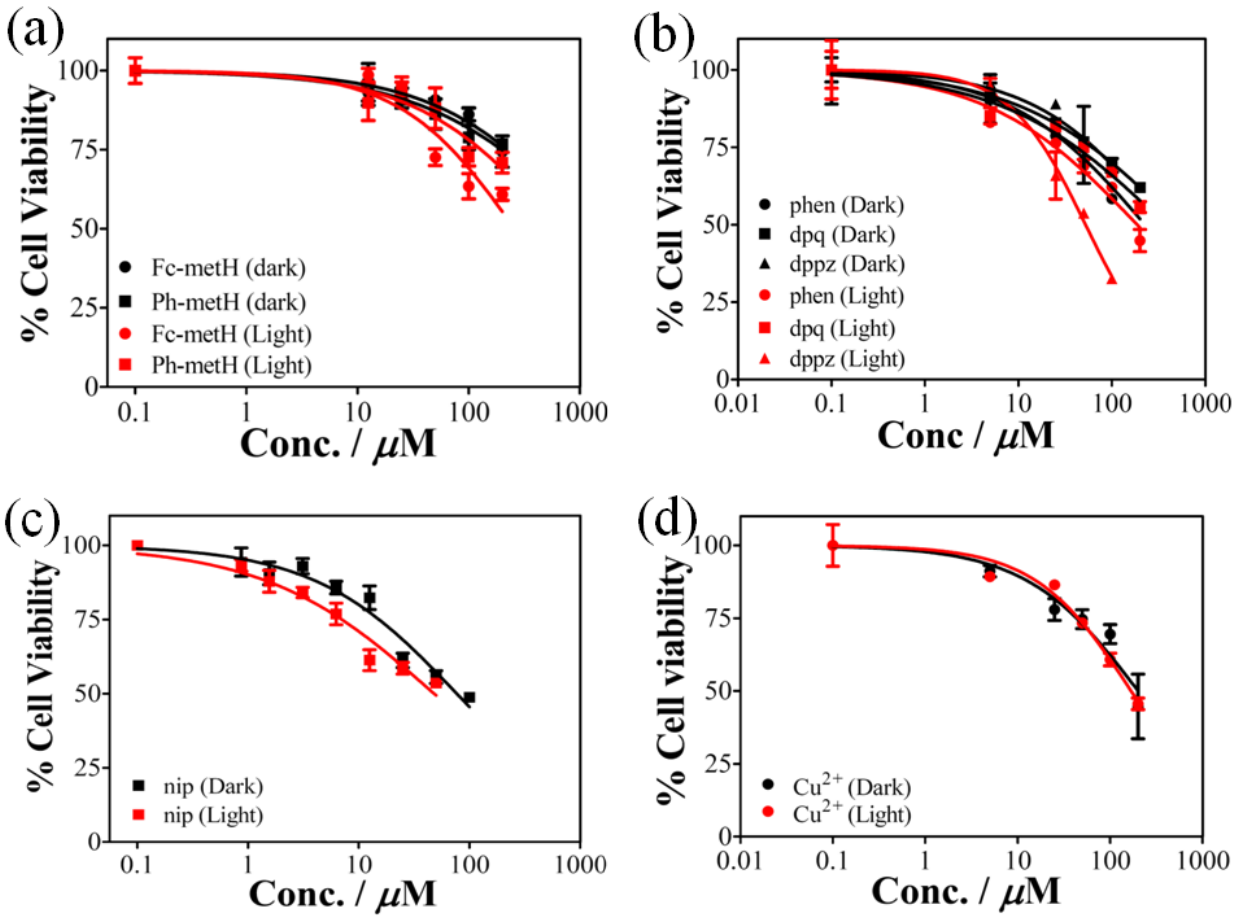

Figure S21. Cell viability plots showing cytotoxic effect of (a) Fc-metH and Ph-metH ligands; (b) phen, dpq and dppz ligands; (c) nip ligand and (d) $Cu(NO_3)_2{\cdot}3H_2O$ in HeLa cells in dark (black symbols) and in the presence of visible light (red symbols, 400-700 nm, 10 *J* cm^{-2}).

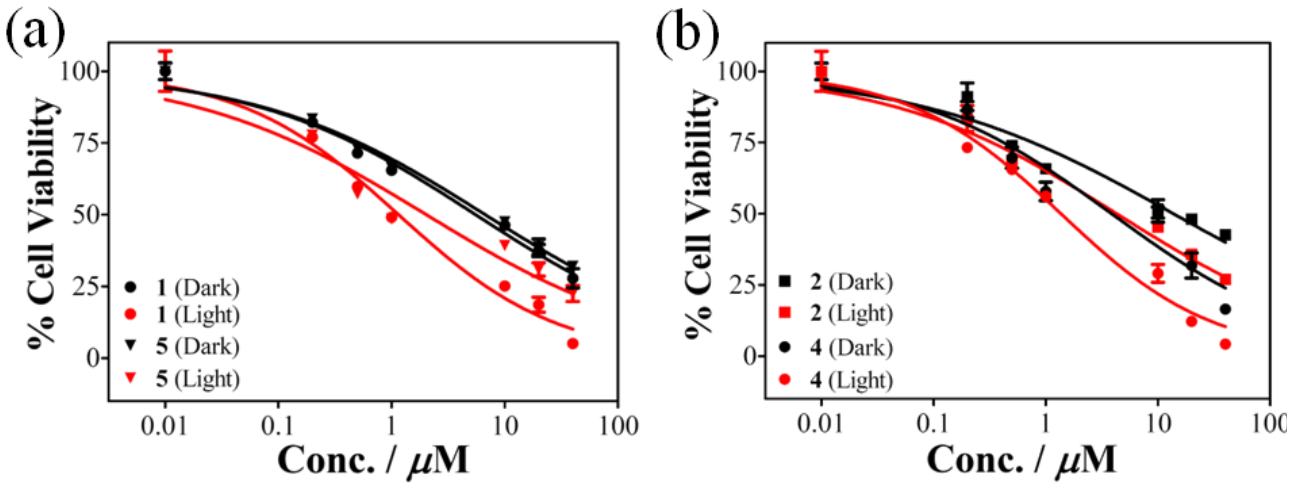

Figure S22. Cell viability plots showing cytotoxic effect of (a) complexes **1** and **5** and (b) complexes **2** and **4** in MCF-7 cells in dark (black symbols) and in the presence of visible light (red symbols, 400-700 nm, 10 *J* cm^{-2}).

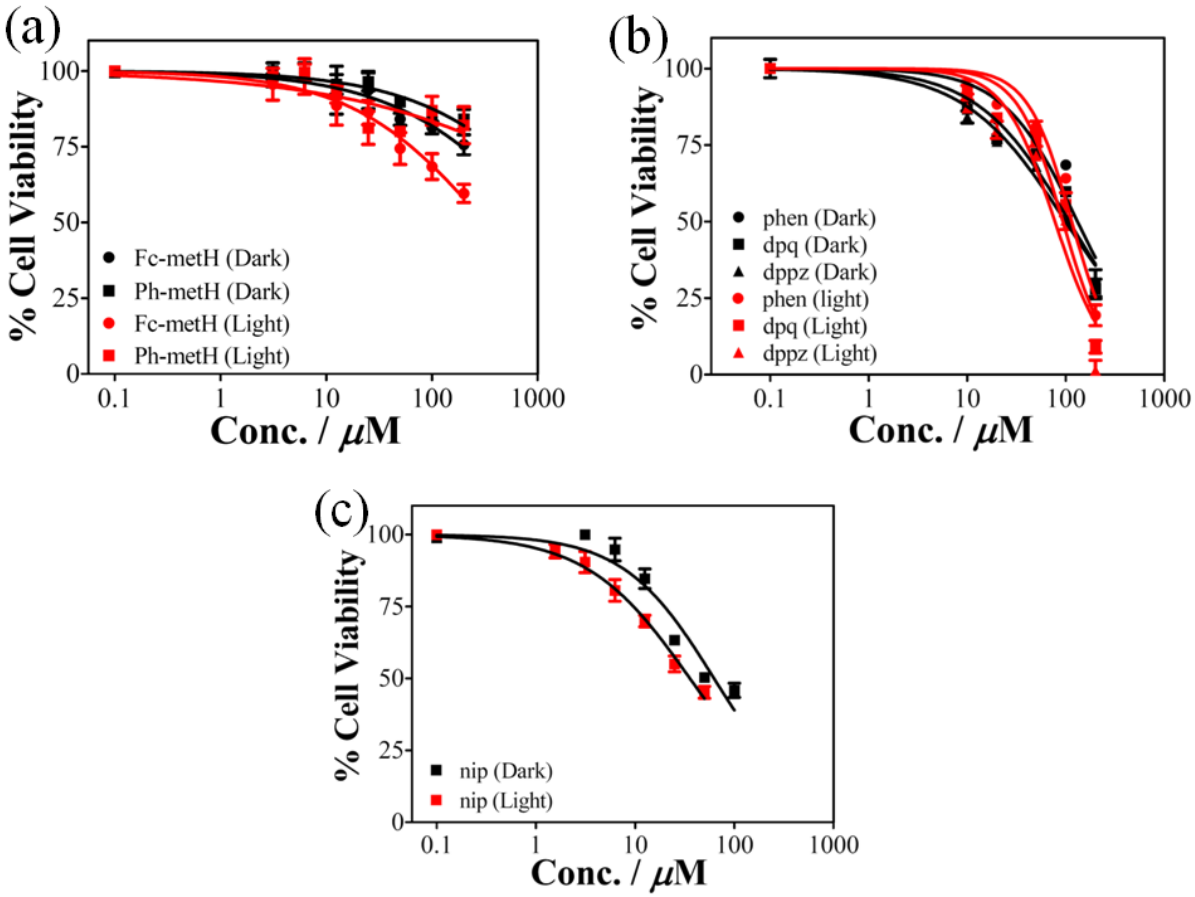

Figure S23. Cell viability plots showing cytotoxic effect of (a) Fc-metH and Ph-metH lignads; (b) phen, dpq and dppz ligands and (c) nip ligand in MCF-7 cells in dark (black symbols) and in the presence of visible light (red symbols, 400-700 nm, 10 *J* cm^{-2}).

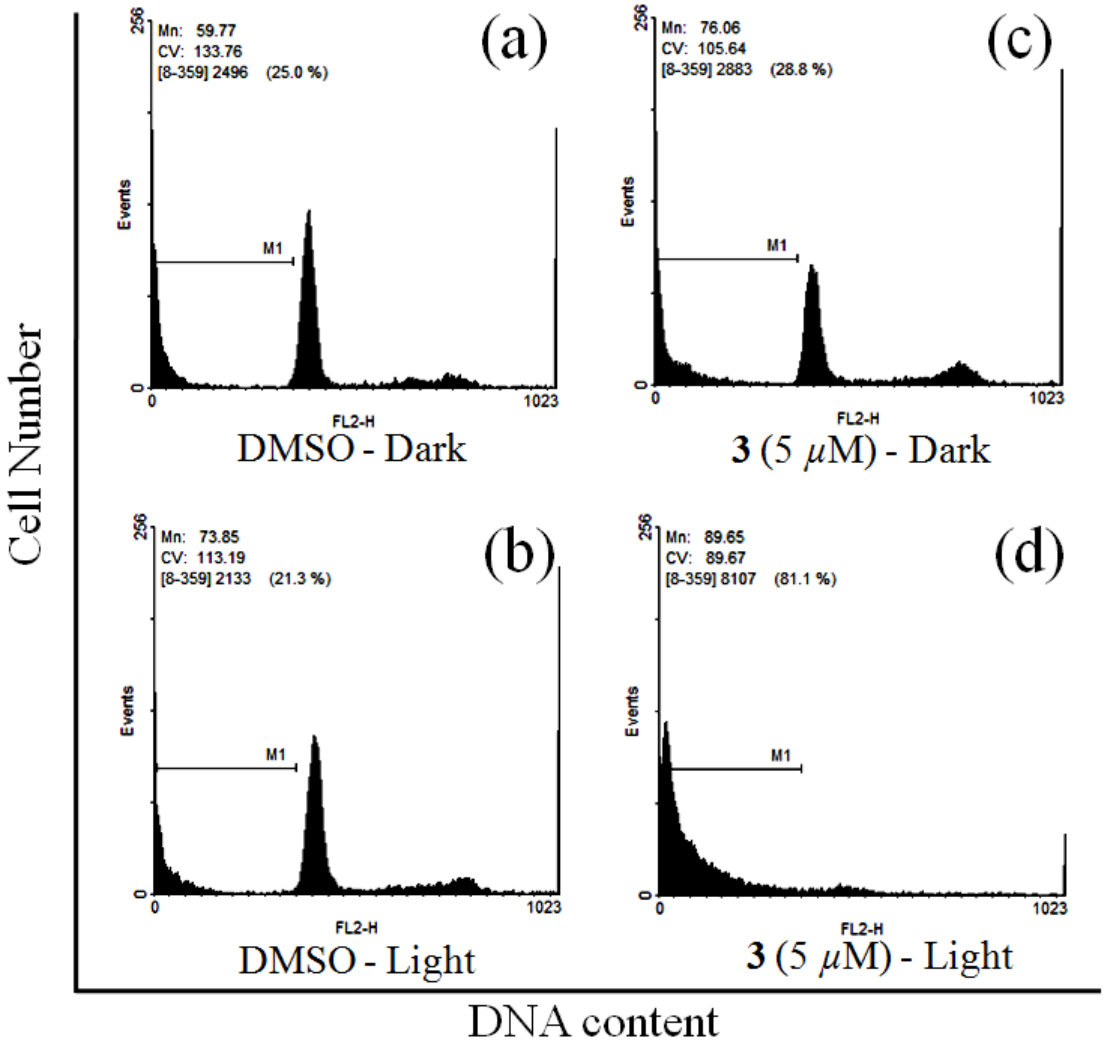

Figure S24. Complex **3** induced apoptotic cell death by flow cytometric analysis: (a) control cells in the dark, (b) control cells exposed to visible light (400-700 nm, 10 *J* cm^{-2}), (c) cells treated with complex **3** in the dark and (d) cells treated with complex **4** (5 μM) exposed to visible light (400-700 nm, 10 *J* cm^{-2}).

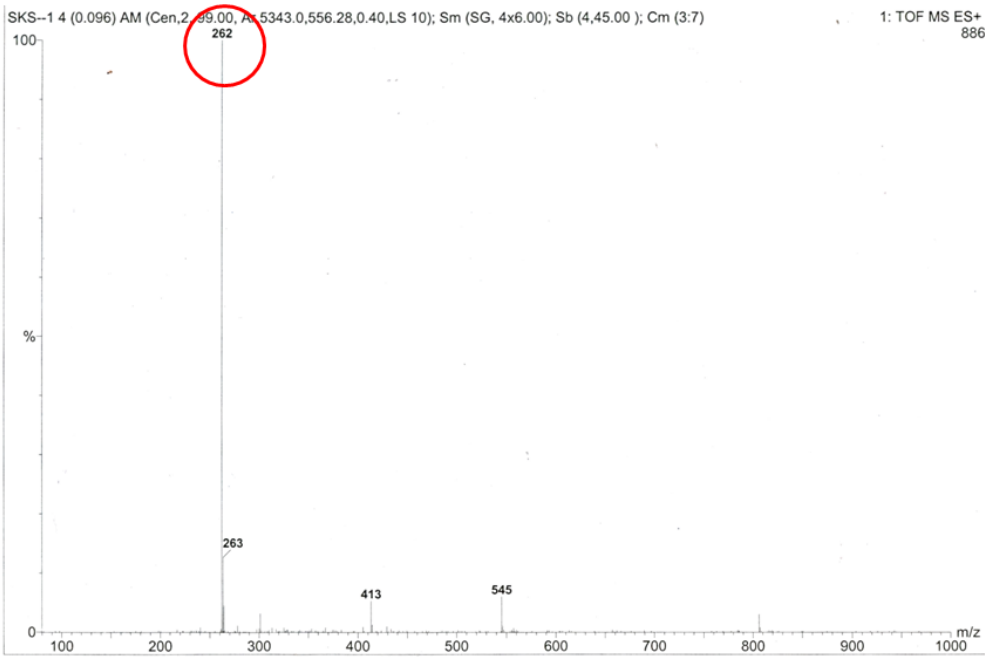

Figure S25. The ESI-MS spectrum of Ph-metH ligand in aqueous MeOH showing prominent peak corresponding to [M+Na^{+}] at 262 (m/z).

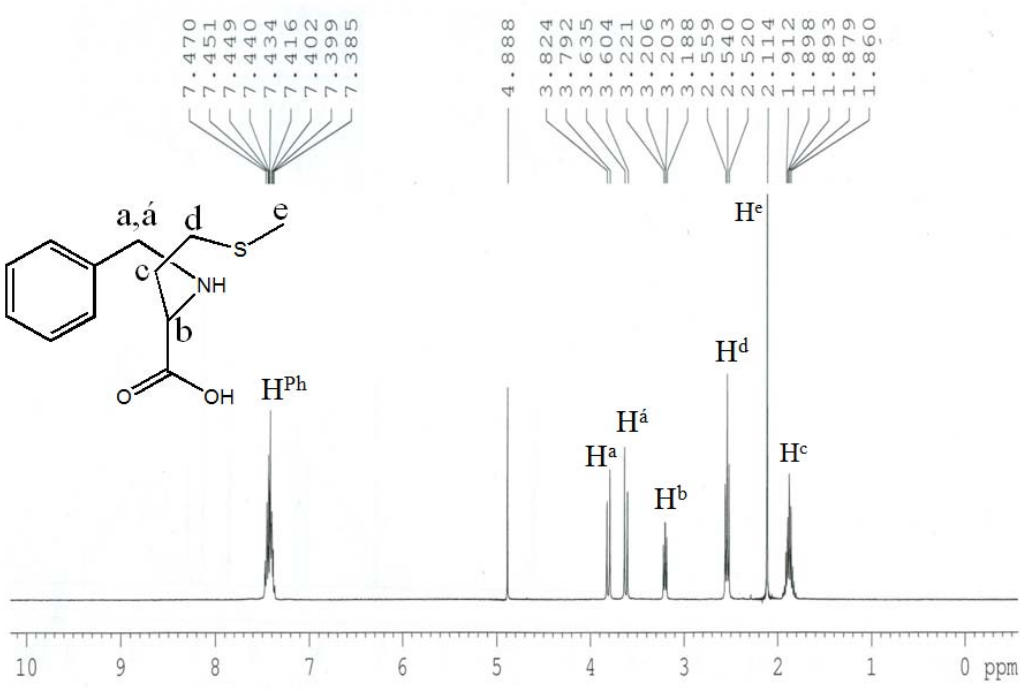

Figure S26. The ^{1}H-NMR spectrum of Ph-metH ligand in D_2O

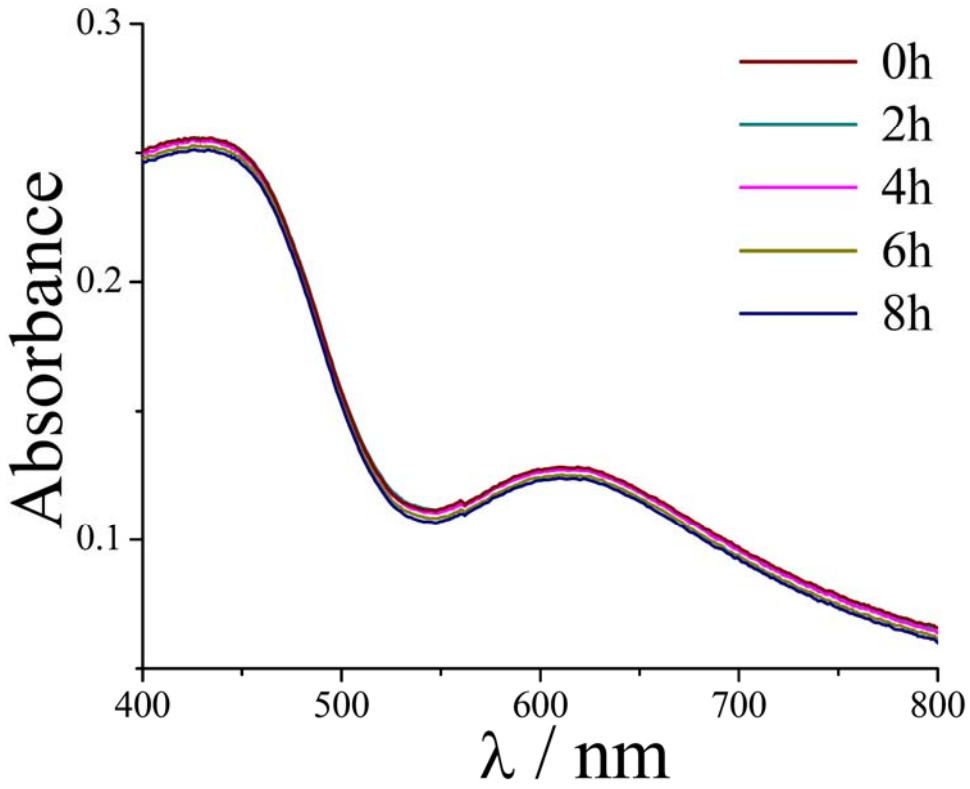

Figure S27. Spectral traces in the visible region of complex **1** (1mM) in the presence of Bovine Serum Albumin (BSA) (10 μM) at various time intervals. No apparent changes in the spectrum indicate the stability of the complex in the presence of BSA.

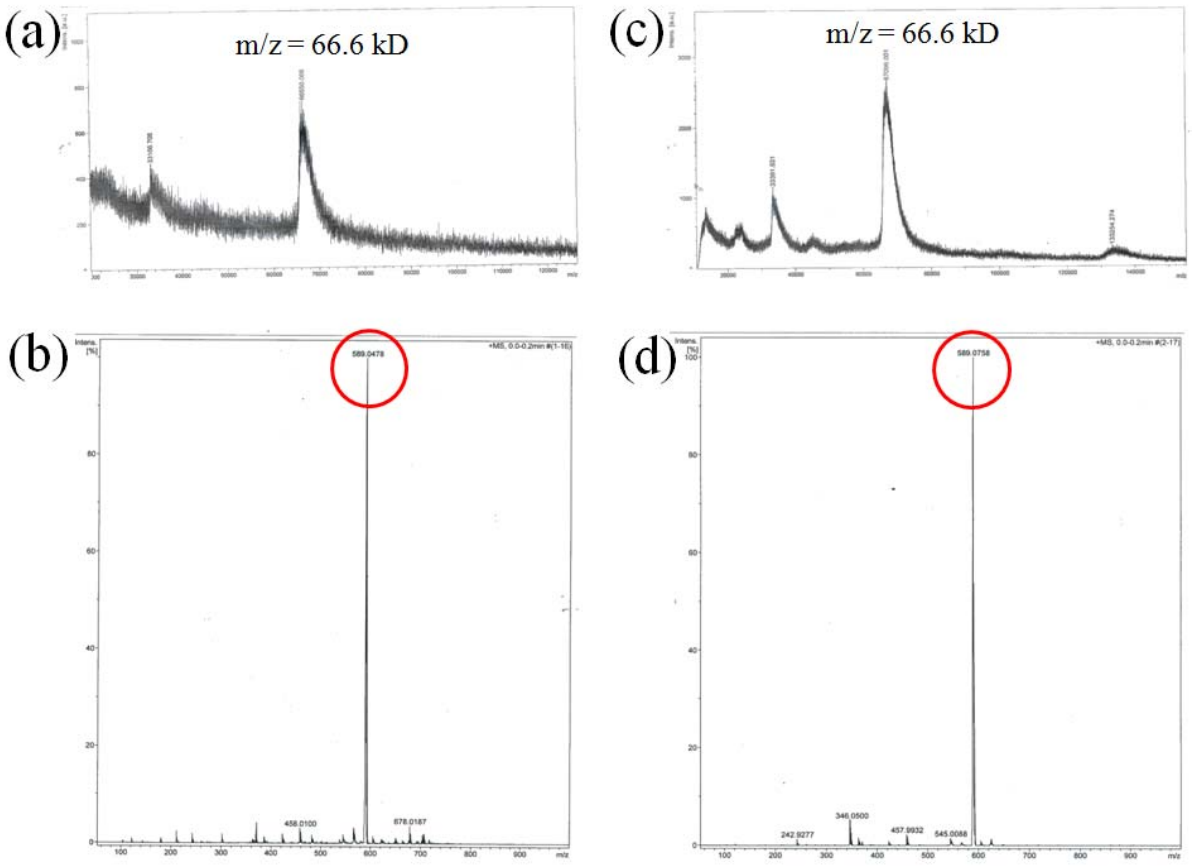

Figure S28. MALDI-TOF MS and ESI-MS spectra of a mixture of Bovine Serum Albumin (BSA) (10 μM) and complex **1** (200 μM) just after mixing (a and b) and after 8 h (c and d). The peaks at m/z = 66.6 kD and 589 correspond to BSA and $[M-(NO_3^-)]^+$ of complex **1**, respectively. No apparent change in the ESI-MS indicates the stability of the complex in the presence of BSA.

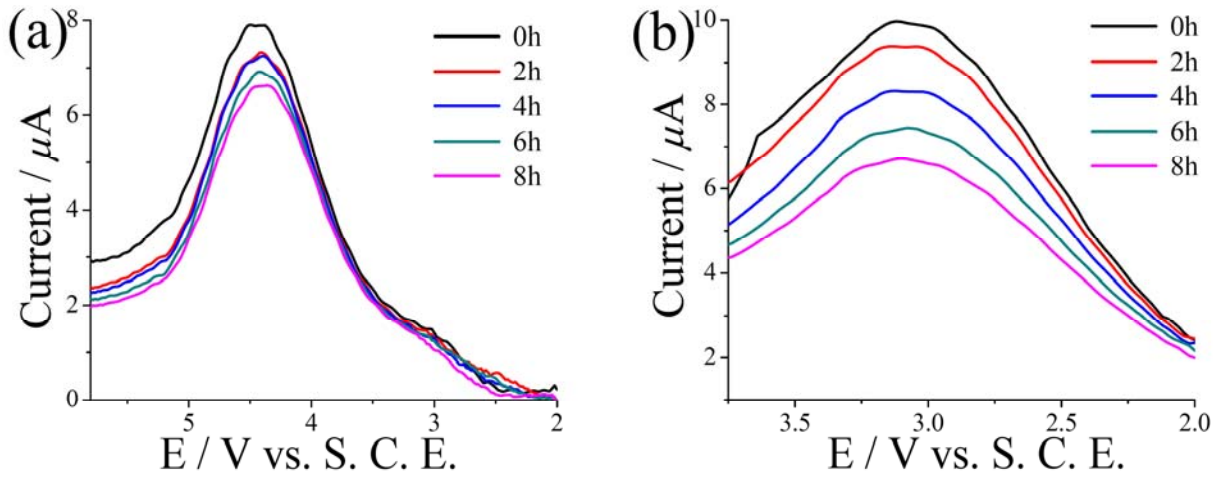

Figure S29. Differential pulse voltammograms (DPV) of (a) complex **1** (2 mM) in the presence of Bovine Serum Albumin (BSA) (10 μM) at different time points; (b) Fc-metH ligand (2 mM) in the presence of BSA (10 μM) at the same time points in DMF/H_2O (1:4 v/v)-0.1 M TBAP (scan rate: 5 mV s^{-1}). No apparent change in DPVs indicates that in the presence of BSA, Cu^{2+} is not undergoing decomplexation (leaching) from the complex leaving Fc-metH ligand free in solution atleast upto 8 h.

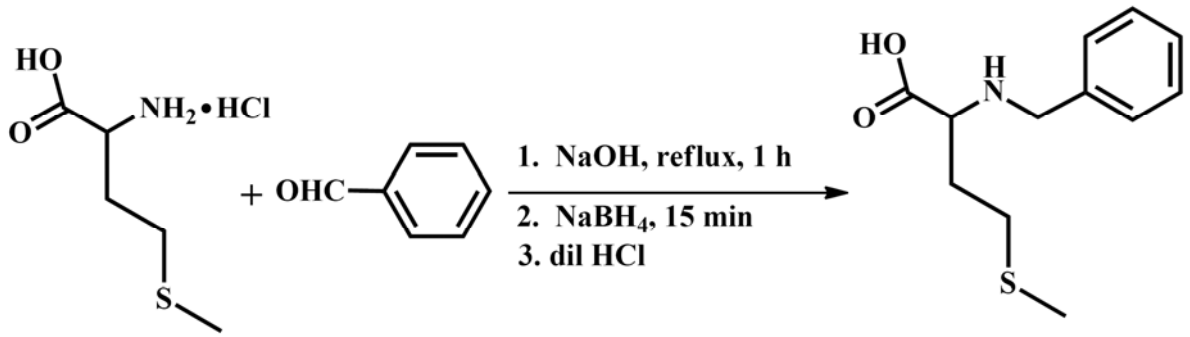

Scheme S1. Synthetic scheme for the ligand Ph-metH.

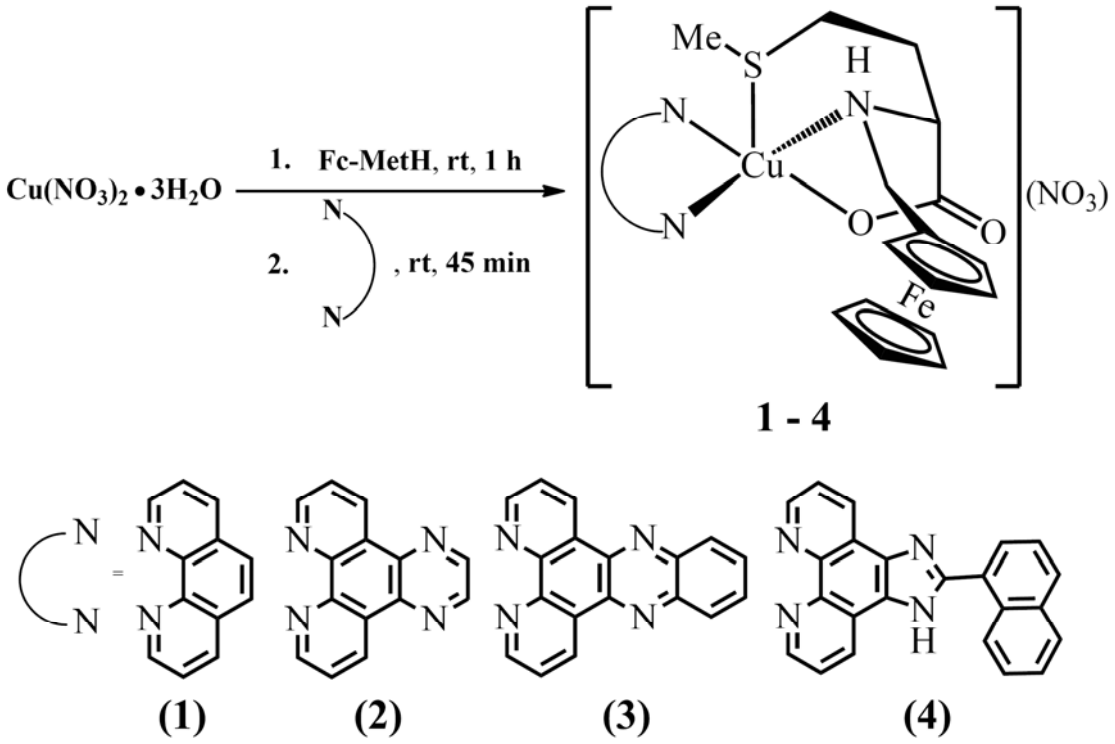

Scheme S2. Synthetic scheme for the complexes **1-4**.

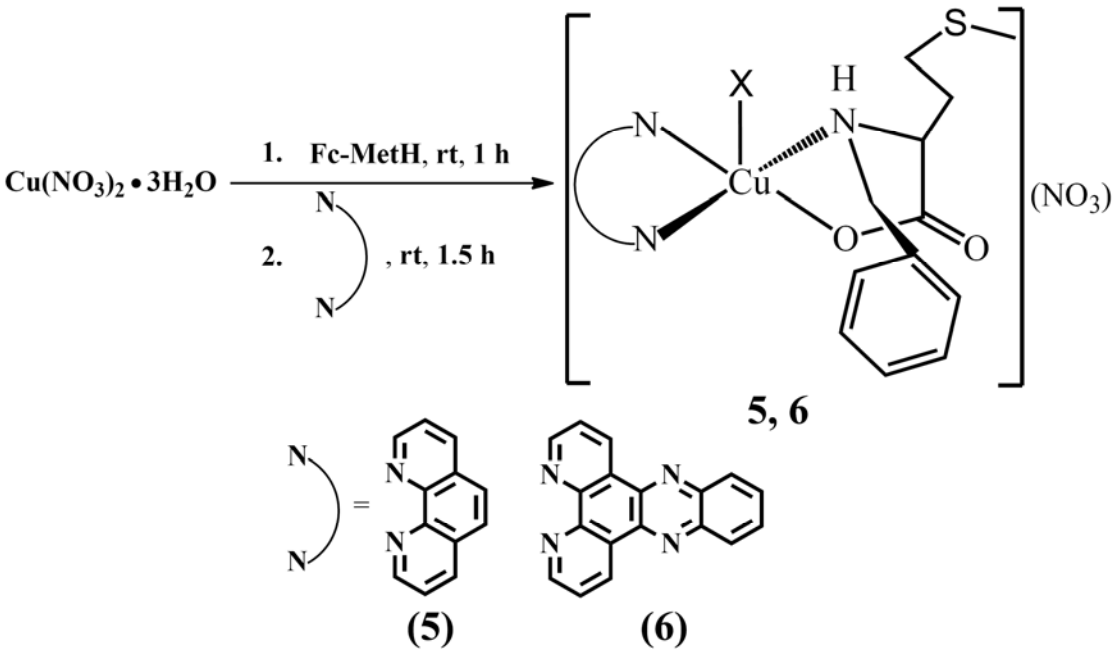

Scheme S3. Synthetic scheme for the complexes **5** and **6** (X = carboxylate oxygen in the solid state and H_2O in an aqueous phase).